

1     **On the local day time urban heat island of an idealized 2D city**

2                     P.J.C. SCHRIJVERS \* H.J.J. JONKER, S.R. DE ROODE

*Faculty of Civil Engineering and Geotechnology, Delft University of Technology, Stevinweg 1, 2628CN Delft, The Netherlands*

*J.M. Burgers Centre for Fluid Dynamics, Julianalaan 136, 2628BL, The Netherlands*

3                     S. KENJEREŠ

*Faculty of Applied Sciences, Delft University of Technology, Julianalaan 136, 2628BL, The Netherlands*

*J.M. Burgers Centre for Fluid Dynamics, Julianalaan 136, 2628BL, The Netherlands*

---

\* *Corresponding author address:* Patrick Schrijvers, Delft University of Technology, Stevinweg 2, 2628CN, Delft.

E-mail: p.j.c.schrijvers@tudelft.nl

5 This study investigates the energy budget of the day time urban heat island effect for an  
6 idealized 2D geometry. A transient building-resolving simulation model has been developed,  
7 which computes radiative transfer, conduction, ventilation and mean radiant temperature  
8 at a 1 meter spatial resolution. A range of canyon height to width ratios ( $H/W$ ) are used,  
9 ranging from  $H/W=0.0$ , 0.5, 1.0, 2.0 and 4.0. Results indicate that absorbed short wave  
10 radiation has the largest contribution to the energy budget, and exceeds that of the flat  
11 terrain due to increased multiple reflections for lower  $H/W$  ratios. The long-wave trapping  
12 effect has the second largest contribution but becomes relatively larger with increasing  $H/W$   
13 ratio. Sensible heat has two distinct regimes, where for  $H/W \leq 1.0$ , the canyon is well mixed.  
14 For deeper canyons, a stable stratification is formed in the lower part of the canyon. The  
15 latent heat flux process reduces the surface temperature by as much as 12K, which can  
16 lead to different vortex dynamics and increase air temperature at street level. Mean radiant  
17 temperature is dominated by short wave radiation, and for  $H/W \leq 1.0$  exceeds that of the flat  
18 terrain. For deeper canyons, shading and the reduced sky view factor reduce mean radiant  
19 temperature quickly. Surface temperature and mean radiant temperature are closely related,  
20 since both are largely dominated by radiative properties. No straightforward link was found  
21 between surface temperature and air temperature, since air temperature is dependent on  
22 forced convection and buoyancy forces. Large variations are found within one street canyon.

# 1. Introduction

The night time Urban Heat Island (UHI) phenomena is a well known effect, showing a reduced decrease in air temperature of 1 to 10 Kelvin compared to the rural environment (Oke 1981; Klysik and Fortuniak 1999; Kim and Baik 2004; Grimmond 2007; Steeneveld et al. 2011). However, the day time UHI effect is much smaller and can even be negative (Taha 1997; Klysik and Fortuniak 1999; Ryu and Baik 2012). The UHI effect is defined as the air temperature difference between the urban and rural environment, but is often a difficult parameter to measure. In part this is due to the extreme difficulty in observing the urban boundary layer at multiple locations. When interpreting profiles from a single measurement location, the effect of advection across the heterogeneous urban surface should also be taken into account (Barlow 2014). To overcome this problem, surface temperature can be used which can be obtained from (for instance) satellite data and gives an overview over a large domain (city scale). Large differences between the urban and rural environment can be observed during the day, up to 10K in the summer (Klok et al. 2012) and 7K annually averaged (Peng et al. 2012). Differences are not only present between the urban and rural environment, but also within the city and even within a single street canyon due to (amongst others) shading effects and changes in the sensible heat flux, that can be between 25 - 40% within a neighbourhood area (Schmid et al. 1991). In addition to the air temperature and surface temperature, there is a third temperature which is interesting to look at during day time: mean radiant temperature. This is a radiative temperature indicative for the radiative comfort, and is used in the computation of apparent temperatures like the Physiological Equivalent Temperature PET (Höppe 1999) and the Universal Temperature Climate Index UTCI (Fiala et al. 2012).

These different temperatures are linked through radiative and convective processes, but it is hard to know the exact conversion a priori. Therefore, this study will focus not only on air temperature, but also on surface temperature and the mean radiant temperature.

Klysik and Fortuniak (1999) studied the atmospheric UHI effect of Lodz, Poland by using

fixed point measurements from a weather station in the city centre over a long time period. It was found that on days when the weather is dominated by solar radiation, there are big thermal contrasts within the city. Close to the ground in areas with high building density, the air may be cooler than the rural environment due to shading of the ground surface. Roofs play an important role in that scenario, since they can form a layer of warm air, creating a local stable inversion layer, thereby limiting the vertical exchange of air in the street canyons.

In an overview study by Taha (1997), effects of changing surface albedo and latent heat release are discussed. It was found that altering the surface albedo from 0.25 to 0.40 could reduce localized afternoon air temperatures as much as 4K. The study also indicated that vegetation canopies can create 'oases' that are 2 to 8K cooler than their surroundings due to increased evaporation of water.

A systematic study of different physical processes was performed with the meso-scale model WRF (Weather and Research Forecasting model) by Ryu and Baik (2012), where three main causative factors were identified: anthropogenic heat, impervious surfaces (which included the reduction in surface moisture availability and increased thermal inertia) and 3D urban geometry (additional heat stored in vertical walls, radiative trapping and reduction in ventilation). The building height (H) over street width (W) ratio (H/W) used in this study is H/W=1.0. Their study indicated that during day time the impervious surfaces contributes most to the urban heat island (+2.1K), while the 3D urban geometry actually cools the city (-0.5K). In total, they found that the air temperature inside the city is 2.1K warmer than the surrounding rural area.

When mean radiant temperature is considered, Lindberg et al. (2008) indicated that it can vary largely during the day, with a peak value of 328K. This was obtained from measurements in Goteborg (57° 42' N, 11° 58' E) on a large open square in the city centre. Results for measurements in a courtyard showed a mean radiant temperature of 290K when the measurement location was shaded. If the measurement location was directly illuminated by the sun, mean radiant temperature peaked at 300K, showing not only the large spatial,

but also temporal variability.

The goal of this study, conducted within the Dutch Climate Proof Cities consortium (Albers et al. 2014) is to find the mechanisms that control day time surface temperature, air temperature and mean radiant temperature on the scale of individual obstacles. The micro-scale model discussed in Schrijvers et al. (2014) is used, which couples a Monte-Carlo radiative transfer model, 1D heat conduction equation for the conductive heat flux into buildings and ground and a Computational Fluid Dynamics (CFD model) for the convective heat fluxes. A similar case set-up is used as in Schrijvers et al. (2014), where a range of H/W ratios are considered (0.0, 0.5, 1.0, 2.0, 4.0) as well as different physical mechanisms. Starting from radiative equilibrium, complexity is added by including the conductive heat flux, sensible heat flux and finally the latent heat flux.

Section 2 will shortly discuss the model and case set-up. Results will be discussed in section 3. Our final goal is two-fold: 1) disentangle the mechanisms involved in the urban heat budget and 2) study the relation between surface temperature, air temperature and mean radiant temperature.

## 2. Methods and case set-up

The transient building-resolving model used in this study is the same as used in Schrijvers et al. (2014). Therefore, only a short description will be given here. Extensions of the model for this study are discussed in more detail.

### *a. Radiative transfer*

Radiative transfer is computed by a Monte-Carlo model, where photon paths are computed for four radiative components: 1) diffuse short wave radiation, 2) direct short wave radiation, 3) long wave radiation emitted by the sky and 4) long wave radiation emitted by a surface.

Photon packets are emitted at the top of the domain (radiation types 1, 2 and 3) or at a surface (radiation type 4). A photon packet (consisting of multiple photons) is used to increase convergence speed. The photon packet's trajectory is computed from cell face to cell face until a surface is hit. A fraction of the energy  $(1 - \xi)$  is absorbed, which is related to the albedo (short wave radiation) or emissivity (long wave radiation). The remainder of the energy travels further in a random direction, which is computed based on the Lambertian cosine law. Photon packets with less than 0.5% of the initial energy are discarded to decrease computation time. Periodic boundary conditions are applied, such that photon packets can only leave the domain through the top boundary. The magnitude of the short wave radiative flux is based on a parametrisation proposed by Skartveit et al. (1998). In this model, short wave radiation and the splitting between direct and diffuse radiation is based on the solar constant  $I$ , Julian date  $d_n$ , latitude, longitude, Linke turbidity factor  $T_L$  (Kasten 1996) and the solar zenith angle  $\gamma$ , which is computed following Iqbal (1983). Although the parameterisation allows for cloudy skies, this is not taken into account in the current model, which results in a maximum direct short wave radiative flux of  $833.1 \text{ Wm}^{-2}$  and a maximum diffuse short wave radiative flux of  $84.2 \text{ Wm}^{-2}$  at mid day for this study.

The emitted long wave radiation by the sky is computed following the Stefan-Boltzmann law, where it is assumed that all long wave radiation is emitted at the top of the domain. The emissivity of the sky is computed following Prata (1996) as

$$\epsilon_{\text{sky}} = 1 - \left(1 + c \frac{e_a}{T_a}\right) \times \exp \left[ -\sqrt{1.2 + 3.0 \times c \frac{e_a}{T_a}} \right] \quad (1)$$

where  $e_a$  is the water vapour pressure (in hPa),  $T_a$  the air temperature (in K) and  $c = 46.5 \text{ K/hPa}$  is constant based on typical values for the water vapour scale height and temperature lapse rate (Prata 1996).

Kirchoff's law is assumed for broadband radiation, indicating that the same value is used for reflection and emission of long wave radiation at the surface ( $\alpha = \epsilon$ ).

b. Mean radiant temperature ( $T_{\text{mrt}}$ )

In addition to the existing model, computation of the mean radiant temperature ( $T_{\text{mrt}}$ ) is added. The mean radiant temperature is computed by

$$T_{\text{mrt}} = \sqrt[4]{\frac{S_{\text{str}}}{\epsilon_{\text{p}}\sigma}} \quad (2)$$

where  $S_{\text{str}}$  is the local mean radiant flux density,  $\epsilon_{\text{p}}$  the emissivity of the human body (with a standard value of 0.97) and  $\sigma$  the Stefan-Boltzmann constant.

The mean radiant flux density can be regarded as the amount of radiation (both short wave and long wave) that is absorbed by a person. It is computed by

$$S_{\text{str}} = \alpha_{\text{k}} \sum_{i=1}^6 K_i F_i + \epsilon_{\text{p}} \sum_{i=1}^6 L_i F_i \quad (3)$$

where  $\alpha_{\text{k}}$  is the albedo of the human body (with a standard value of 0.7),  $K_i$  the total short wave radiative flux,  $L_i$  the total long wave radiative flux and  $F_i$  a geometric factor representing a standing human body. A summation is done over the 6 cardinal points, where the geometric factor is set to 0.22 for radiation hitting the human body from the east, west, south and north direction, while the geometric factor is set to 0.06 for radiation entering from the top and bottom. Since a 2D setting is used in this study, the north and south component are non-existing, and are taken as the average of the east and west component.

Instead of computing  $T_{\text{mrt}}$  at each time step, this is done as a post processing action after the full simulation has converged.  $T_{\text{mrt}}$  is a function of all radiative components (and thus also surface temperature, due to emitted long wave radiation by the surface). The surface temperature for a specific time-step is used, and all radiative components are computed. Recomputing comes with the additional cost of computation time, but is less memory intensive.

Within the Monte-Carlo model, computing the mean radiant flux density is a question of book keeping, where the amount of radiative flux entering a grid cell is stored per direction

and radiation type.

*c. Mean radiant temperature validation*

The computation of  $T_{\text{mrt}}$  is validated against analytical results by Madronich (1987). In this paper, a clear derivation of the actinic flux (also called integrated density or flux density) is given and analytical data is presented.

Validation of the Monte-Carlo model is conducted by considering two cases. In the first case direct radiation of  $800 \text{ Wm}^{-2}$  is emitted with a solar zenith angle of 0 degrees onto a diffuse scattering surface with albedo  $\alpha=1$  (no absorption). Madronich (1987) derived that the upward reflected energy equals that of the downward radiative energy ( $800 \text{ Wm}^{-2}$  in this case), while the sideways components (east and west flux density) are half of the incoming energy ( $400 \text{ Wm}^{-2}$ ). Results are shown in Fig. 1, where the top left panel shows spatial information on the eastward flux for the whole 2D domain, while the bottom left panel shows extracted lines for all flux directions. The top left plot shows that the eastward component is  $400 \text{ Wm}^{-2}$  (50%) of the incoming direct radiation for the whole domain. There are small spatial differences due to the Monte-Carlo method, which are around  $2 \text{ Wm}^{-2}$ . These fluctuations will decrease with increasing number of photons. The bottom left panel shows extracted lines within this domain, where the top and bottom flux are  $800 \text{ Wm}^{-2}$ , while the east and westward flux are  $400 \text{ Wm}^{-2}$ , as expected from Madronich.

The second case is conducted by emitting diffuse radiation ( $100 \text{ Wm}^{-2}$ ) from the top of the domain onto the same diffuse scattering surface used in the previous case. Since there is now also diffuse radiation from the top, it is derived that the radiative flux density is equal in all directions. This is shown in the right panels of Fig. 1, where the top right panel shows the spatial differences for the eastward flux, while the bottom panel shows the extracted lines. Spatial differences show indeed an uniform distribution of  $100 \text{ Wm}^{-2}$  with fluctuations of  $0.5 \text{ Wm}^{-2}$ . Also the line plots (bottom right) show that all fluxes have the same magnitude of  $100 \text{ Wm}^{-2}$ .



173 *d. Conductive heat flux*

174 The conductive heat transfer is computed by the temperature gradient inside the urban  
175 material

$$G_i = \lambda \frac{\partial T}{\partial x_i} \quad (4)$$

176 where  $\lambda$  is the thermal conductivity of the material. The temperature profile is computed  
177 by the 1D heat conduction equation

$$\frac{\partial T}{\partial t} = k_d \frac{\partial^2 T}{\partial x_i^2} \quad (5)$$

178 where  $k_d$  is the thermal diffusivity, based on the conductivity  $\lambda$ , density  $\rho$  and specific heat  
179  $C_v$  of the ground or obstacle

$$k_d = \frac{\lambda}{\rho C_v} \quad (6)$$

180 A zero flux boundary condition is used at a distance  $\Delta x$  into the ground or obstacle. Fifty  
181 layers are used, along with a time step of 1 second. The second boundary condition that  
182 is used is the surface temperature. Although a time step of 1 second is used to compute  
183 the temperature profile, surface temperature is updated every 6 minutes, indicating that the  
184 conductive heat flux only updates the first boundary condition at this time period.

185 *e. Computational Fluid Dynamics (CFD) model*

186 Ventilation effects are computed by an in-house developed CFD model (Kenjeres and  
187 Hanjalic 1999, 2006, 2009; Kenjeres and ter Kuile 2013). This model uses the Transient  
188 Reynolds-Averaged Navier-Stokes (T-RANS) equation to solve the wind field and air tem-  
189 perature distribution.

190 The unknown Reynolds stress  $\overline{u_i u_j}$  is computed by using the  $k - \epsilon$  turbulence model,  
191 which relates the turbulent stresses to the turbulent kinetic energy (TKE) and dissipation  
192 of TKE.

$$\nu_t = C_\mu k \tau \quad (7)$$

$$\begin{aligned} \frac{\partial k}{\partial t} + U_j \frac{\partial k}{\partial x_j} = \frac{\partial}{\partial x_j} \left[ \left( \nu + \frac{\nu_t}{\sigma_k} \right) \frac{\partial k}{\partial x_j} \right] - \\ \overline{u_i u_j} \frac{\partial U_i}{\partial x_j} - \epsilon - g_i \beta \overline{\theta u_i} \end{aligned} \quad (8)$$

$$\begin{aligned} \frac{\partial \epsilon}{\partial t} + U_j \frac{\partial \epsilon}{\partial x_j} = \frac{\partial}{\partial x_j} \left[ \left( \nu + \frac{\nu_t}{\sigma_\epsilon} \right) \frac{\partial \epsilon}{\partial x_j} \right] + \\ \frac{\epsilon}{k} \left( C_{\epsilon 1} \overline{u_i u_j} \frac{\partial U_j}{\partial x_i} - C_{\epsilon 2} \epsilon + C_{\epsilon 3} g_i \beta \overline{\theta u_i} \right) \end{aligned} \quad (9)$$

where  $k$  is the turbulent kinetic energy,  $\epsilon$  is the dissipation and  $C_\mu$ ,  $\sigma_k$ ,  $\sigma_\epsilon$ ,  $C_{\epsilon 1}$ ,  $C_{\epsilon 2}$  and  $C_{\epsilon 3}$  are constants, taken from the standard  $k - \epsilon$  model (see table 1).

It is known that the standard  $k - \epsilon$  model over predicts the amount of turbulent kinetic energy at stagnation points (Durbin 1996). To compensate for this, the Durbin time-scale limiter  $\tau$  is used, which bounds the turbulent viscosity and therefore also the turbulent kinetic energy.

$$\tau = \min \left[ \frac{k}{\epsilon}, \frac{0.6}{\sqrt{6} C_\mu |S|} \right] \quad (10)$$

where  $|S|$  the strain rate tensor.

Next to the velocity field, the temperature field is solved by using the T-RANS equations. The unknown turbulent heat flux  $\overline{\theta u_j}$  requires modelling, and is solved by using the Simple Gradient Diffusion Hypothesis (SGDH), where the turbulent flux is related to the temperature gradient.

$$-\overline{\theta u_i} = \frac{\nu_t}{\text{Pr}_t} \frac{\partial T}{\partial x_i} \quad (11)$$

where  $\text{Pr}_t$  is the turbulent Prandtl number, set to 0.86.

This allows us to compute the sensible heat flux following

$$H_i = \rho c_p \overline{\theta u_i} \quad (12)$$

where  $\rho$  is the density of air ( $1.208 \text{ kgm}^{-3}$ ) and  $c_p$  the specific heat capacity of air ( $1004 \text{ Jg}^{-1}\text{K}^{-1}$ ).

#### *f. Latent heat flux*

As an extension of the model, the latent heat flux process is taken into account which is computed by using the Bowen ratio  $\psi$ . This couples the sensible heat flux to the latent heat flux in a simple but effective manner.

$$Le_i = \frac{H_i}{\psi} \quad (13)$$

The latent heat flux process is only added if the sensible heat flux is positive  $H_i \geq 0$ . Negative latent heat flux is not taken into account.

#### *g. Integrated energy balance model*

All sub-models compute a part of the total surface energy balance, which dictates that all fluxes should balance

$$\begin{aligned} SW_{\text{dir}} + SW_{\text{dif}} + LW_{\text{sky}} + LW_{\text{trap}} \\ = LW_{\text{out}} + H + Le + G \end{aligned} \quad (14)$$

where  $SW_{\text{dir}}$  is the absorbed direct component of short wave radiation,  $SW_{\text{dif}}$  the absorbed diffuse short wave component,  $LW_{\text{sky}}$  the absorbed long wave radiation emitted by the sky,  $LW_{\text{out}}$  is the emitted long wave radiation by the surface,  $LW_{\text{trap}}$  the long wave radiation emitted by one surface and absorbed by another surface,  $H$  the sensible heat flux (where a

positive flux is heating of air),  $Le$  the latent heat flux (positive is evaporation of water) and  $G$  the conductive heat flux (positive is adding energy to the underlying layers). Note that multiple reflections are included in the terms of  $SW_{\text{dir}}$ ,  $SW_{\text{dif}}$  and  $LW_{\text{sky}}$ .

The controlling parameter for the surface fluxes is the surface temperature, where a skin layer is assumed to prevent large variations in surface temperature in time

$$\Delta_{\text{skin}} \rho_{\text{skin}} C_{\text{v,skin}} \frac{\partial T_s}{\partial t} = \Gamma \quad (15)$$

where  $\Gamma$  is the flux imbalance resulting from the surface energy balance and  $\Delta_{\text{skin}} \rho_{\text{skin}} C_{\text{v,skin}} = 0.01$ .

For a time step, all fluxes in the surface energy balance are computed based on the surface temperature of the previous time step. This can result in a small flux imbalance  $\Gamma$ . Based on this imbalance and the old surface temperature, the surface temperature for the new time step is computed.

#### *h. Test cases and research methodology*

To create a test-case suited to study the effect of different physical mechanisms as a function of H/W ratio, an idealized 2D urban geometry is created consisting of 14 obstacles which are spaced  $W=50$  meter apart. By using 14 obstacles, a fully developed flow pattern is found in the last street canyons, indicating that more obstacles would not change the results. All buildings are  $B=25$  meter wide, while building height is varied between 0 meter ( $H/W=0.0$ ), 25 meter ( $H/W=0.5$ ), 50 meter ( $H/W=1.0$ ), 100 meter ( $H/W=2.0$ ) and 200 meter ( $H/W=4.0$ ) (see Fig. 2). By using this wide range of H/W ratio, a detailed analysis can be made on the effect of changing building height.

Next to changes in building height, different mechanisms are switched on and off. Instead of doing a full factor separation analysis like Ryu and Baik (2012), the simplest case of radiative equilibrium is used as a starting point. From this basic case, complexity is added by adding the conductive heat flux mechanism (case 2), sensible heat flux (case 3) and latent

heat flux (case 4) (see table 3).

Ten days are considered in the middle of June, which is the month where the sun is at its maximum zenith angle in the Netherlands. By using ten days, there quasi steady state results are obtained that are independent on the initial conditions (the daily cycle is repetitive). The time step that is used is 6 minutes. Other input parameters are shown in table 2.

Results for Figures 4-7 are plotted according to the inset in Fig. 2, where all vertical surfaces are scaled to a length of 1. This allows us to compare different H/W ratios in a single plot.

### 3. Results

#### *a. Time series*

As a first introduction to the results, time series are shown in Fig. 3 for one point in the middle of the street canyon between obstacle 12 and 13. In this figure, the left panel shows the surface temperature for different H/W ratios and the right panel the total absorbed radiation (both short wave and long wave) for this single point. The radiative equilibrium case 1 is used. Results for the flat plate (H/W=0.0) show a diurnal cycle in surface temperature and absorbed radiation. Surface temperature has a minimal value of 278K during night and peaks at 358K during day. When obstacles are added, the surface temperature for H/W=0.5 exceeds that of the flat plate after mid day (dashed line) due to increased multiple reflections. Also, a clear shading effect can be seen in the absorbed radiation, where absorbed radiation is lower during the night and after sun rise, but peaks very rapidly at mid day. If higher buildings are considered, the point in the centre of the street is shaded throughout the day and surface temperature and absorbed radiation are much lower compared to lower H/W ratios. The diurnal cycle is also less distinct, up to a point for H/W=4.0 where there is almost no daily variation in surface temperature. In this

case, the ground surface receives only a very limited amount of short wave radiation due to shading effects. The small portion of short wave radiation that is absorbed at ground level, comes from multiple reflections and involves much less energy. Note that the surface temperatures for  $H/W=4.0$  are extremely low, since this is only determined by the amount of absorbed radiation. There are no compensating mechanisms to increase surface temperature for this case.

The dashed line in the middle of the last diurnal cycle indicates the point in time where spatial analysis will be conducted on the different fluxes.

#### *b. Radiation*

Fig. 4 displays the absorbed radiative components for mid day for case 1 (radiative equilibrium). Absorbed long wave radiation from the sky is shown in the top left panel, and shows a decreasing absorbed long wave radiation due to the reducing sky view factor with increasing  $H/W$  ratio. For  $H/W=0.5$ , the peak absorbed radiation in the middle of the ground surface is reduced to 75.5% of the radiation absorbed by the flat plate, while the ground surface for  $H/W=4.0$  receives 12% of the radiation absorbed by the flat terrain.

The top right panel shows the absorbed radiation due to long wave trapping. This is  $0 \text{ Wm}^{-2}$  for  $H/W=0.0$ , since there is no absorption at any surface. For  $H/W=0.5$  a clear peak can be seen between the ground and west wall, where the amount of absorbed energy is largest. This is due to the high surface temperature in that region, combined with the corner being the favourable location for long wave trapping. For  $H/W=1.0$ , the long wave trapping effect is stronger at the shaded part of the ground compared to  $H/W=0.5$ . For the other canyon surfaces, there is less absorbed long wave radiation compared to  $H/W=0.5$ . With increasing  $H/W$  ratio, the magnitude of the long wave trapping effect reduces. Although the canyon geometry allows for more long wave trapping, the emitted long wave radiation  $LW_{\text{out}}$  is lower and thus there is less energy that can be trapped.

The total absorbed short wave radiation (direct and diffuse component) is shown in the

bottom left panel. Multiple reflections can be observed at ground level, where the absorbed short wave radiation exceeds that of the flat terrain for  $H/W=0.5$  and  $H/W=1.0$ . Also the shadow location on the ground can be observed, where  $H/W=1.0$  shows more shadowing of the ground surface compared to  $H/W=0.5$ . For  $H/W=2.0$  no part of the ground surface is directly illuminated.

If finally all absorbed radiative components are added, this balances the emitted long wave radiation from the surfaces, due to our assumption of radiative equilibrium. This is shown in the bottom right panel, and shows a clear peak in emitted radiation for  $H/W=0.5$  and  $H/W=1.0$  at the lower corner between ground and west wall, where emitted long wave radiation exceeds that of the flat plate. The long-wave trapping effect and absorbed short wave radiation are about equal in magnitude, while the contribution from absorbed long wave radiation emitted by the sky is much smaller.

### *c. Surface temperature*

From the radiative equilibrium case that is used to display the spatial radiative patterns, more physical mechanisms are added to see the effect on surface temperature. This is shown in Fig. 5 for different  $H/W$  ratios (subplots) and cases (coloured lines). For the flat plate, this shows a surface temperature of 355K for the radiative equilibrium case (case 1). If the conductive heat flux process is added, energy is transferred into the ground, therefore reducing surface temperature by 20K. The sensible heat flux process reduces surface temperature further, due to the free stream air temperature of 293.15K. Latent heat flux is applied with a Bowen ratio of 1.0 (latent and sensible heat flux have the same magnitude), but only if sensible heat flux is positive. This shows a further reduction in surface temperature of 10K, resulting in a surface temperature of 312K for the flat terrain. Due to our assumption of the Bowen ratio, latent heat is a sink of energy where there is only feedback through the reduced surface temperature. This does not only affect the sensible heat flux, but also the conductive heat flux and emitted long wave radiation.

If obstacles are added, the effect of short wave radiation is clearly demonstrated for obstacles with  $H/W=0.5$  and  $H/W=1.0$ , where a part of the ground and the west wall are directly illuminated and therefore have a much higher surface temperature compared to the east wall. This effect is smaller for deeper canyons, where only a portion of the west wall is directly illuminated.

The conductive heat flux shows different behaviour in the sunlit and shaded part of the canyon for  $H/W \leq 1.0$ . If the surface is in the shaded part of the canyon, the conductive heat flux shows only a small effect on surface temperature. On the sunlit part of the canyon, the conductive heat flux mechanisms reduces surface temperature, since energy is transferred into the sub-layers. For  $H/W > 1.0$ , the conductive heat flux raises surface temperature throughout the canyon, except for the small part of the west wall that is directly sunlit.

The surface temperature including the sensible heat flux process (case 3) shows a different pattern for the west and east walls of the canyon. For the west wall, colder ambient air is forced over the warm surface, therefore reducing surface temperature. The air inside the canyon is heated and then forced over the colder (shaded) east wall, showing a much smaller reduction in surface temperature. For  $H/W \geq 2.0$  there is an effect of the sensible heat flux in the top part of the canyon, which was also shown in the night situation (Schrijvers et al. 2014). Forced convection is only able to penetrate the top part of the canyon, showing an increase in surface temperature in that region. Further down into the canyon, wind speeds are small and a stable stratification is apparent, where the sensible heat flux shows almost no contribution to the surface temperature.

If the latent heat flux is added, this only shows an effect on the west wall and the sunlit part of the ground (regions where the sensible heat flux was positive). For  $H/W=0.5$ , the effect is modest, with a reduction in surface temperature of 4K on the west wall. For  $H/W=1.0$  surface temperature is reduced by 12K in the corner between street and west wall compared to the case without the latent heat flux process. The case for  $H/W=2.0$  did not converge to a solution, where the CFD model has large difficulties with the stable



stratification. The simulation shows re-laminarization of the flow field, which violates the basic assumption (a fully turbulent flow) of the  $k - \epsilon$  turbulence model. For  $H/W=4.0$ , the effect of the latent heat release is very small, since the sensible heat flux itself shows only a very small effect inside the canyon.

#### *d. Surface fluxes*

From the surface temperature plots, one can see qualitatively which processes are more important. However, to get a more quantitative view, all individual fluxes are plotted in Fig. 6 for different  $H/W$  ratios (sub plots) and surface fluxes (coloured lines) for case 3 (including conductive and sensible heat flux, but excluding latent heat). The case including latent heat will be discussed later. In this plot, all absorbed radiation entering from the sky ( $SW_{\text{dir}}$ ,  $SW_{\text{dif}}$  and  $LW_{\text{sky}}$ ) are combined. Also note that positive values of  $LW_{\text{out}}$ ,  $G$  and  $H$  indicate a cooling tendency.

This shows that for the flat plate the absorbed radiation contributes  $900 \text{ Wm}^{-2}$  to the surface, while  $600 \text{ Wm}^{-2}$  is emitted through  $LW_{\text{out}}$ . This energy surplus is compensated by the conductive heat flux ( $140 \text{ Wm}^{-2}$ ) and sensible heat flux ( $160 \text{ Wm}^{-2}$ ). The contribution of the conductive heat flux is 15% of the total absorbed radiation, which is slightly higher than the 10% that was found by De Bruin and Holtslag (1982). If the latent heat flux process is added, this 10% is exactly matched.

If cases including obstacles are considered, absorbed radiation remains the dominant factor, although the absorbed radiative fluxes are rapidly decreasing with increasing  $H/W$  ratio. This is largely due to the short wave radiation (see Fig. 4), which is rapidly decreasing. The long wave trapping effect is also reducing with increasing  $H/W$  ratio, but is in general larger than the conductive or sensible heat flux. The long wave trapping effect is relatively increasing with increasing  $H/W$  ratio, where long wave trapping is of equal magnitude as absorbed radiation for  $H/W=4.0$ . This shows the importance of radiation, where all radiative components dominate over the other fluxes.

The conductive heat flux shows very small contributions at the east wall and top part of the west walls. Only at the location where the absorbed radiation peaks is the conductive heat flux active and transferring energy into the canyon material.

The sensible heat flux shows negative values at the east wall for all  $H/W$  ratios, indicating that energy is added to the surface from the passing warmer air. The top west wall shows the contrary, where energy is extracted from the warmer surface. For  $H/W=1.0$ , the shaded part of the ground surface shows no sensible heat flux, indicating that air temperature and surface temperature are equal. For deeper canyons, the sensible heat flux is very close to zero for a larger part of the surface area. This is due to the low levels of turbulence in combination with a small temperature gradient between surface and air, which are caused by the very stable stratification that is formed during night and maintained during the day.

The effect of latent heat release is shown for  $H/W=1.0$  in Fig. 7. Results for the case without latent heat release are shown in the left panel (same as in Fig. 6) and results for case 4 (including latent heat) in the right panel. Adding the latent heat process reduces surface temperature, and therefore also the amount of emitted long wave radiation, especially in the bottom corner between ground and west wall. This impacts the long wave trapping effect directly, since there is less energy that can be trapped. Adding the latent heat flux process also impacts the sensible heat flux, where this is now negative (adding energy to the surface) in the shaded part of the canyon. On the west wall, the sensible heat flux is larger compared to the case without latent heat release, and is almost constant over the vertical wall. This indicates a change in vortex dynamics. As a result, the conductive heat flux is also affected, and is lower in the sunlit part of the canyon compared to the case without latent heat release.

#### *e. Air temperature*

Next to surface temperature, air temperature is of importance, which is a function of wind speed, sensible heat flux and free stream air temperature. Results are shown in Fig. 8, where air temperature and velocity vectors for case 3 (excluding latent heat) are shown. For

400  $H/W=0.5$ , a warm canyon is observed compared to the free stream air temperature, where  
401 one single vortex is present. From the west wall air is heated by the surface and forced  
402 towards the east wall, where the highest air temperature is found.

403 For  $H/W=1.0$  there are two vortices present inside the street canyon. The first vortex  
404 covers the top right part of the canyon, where forced convection is dominant. However, since  
405 the west wall is heated, buoyancy effects become important and create a second counter  
406 rotating vortex in the lower part of the canyon. As a side effect, wind speeds are reduced  
407 due to this battle between forced and natural convection. Air in the bottom part of the  
408 street canyon is cooler than ambient air and can not escape due to the forced convection on  
409 top and the local stable inversion layer that is formed at the top of the canyon. This was  
410 also found in measurements by Klysik and Fortuniak (1999).

411 For  $H/W=2.0$  there is only forced convection in the top part of the canyon and wind  
412 speeds are dramatically reduced towards ground level. As a results, sensible heat flux is  
413 diminished and air temperature is close to surface temperature. Since surface temperatures  
414 of the vertical walls are decreasing towards ground level, a very stable stratification is found,  
415 further preventing mixing of air. This stable situation is self maintaining, although the  
416 location of the top vortex is moving slight downward compared to the night situation. The  
417 same can be found for  $H/W=4.0$ , but even in a more extreme matter with air temperature  
418 close to the ground surface of 240K. This is due to our assumption of a 2D geometry, where  
419 there is only mixing through the top of the canyon.

420 If the case including latent heat is studied (case 4,  $H/W=1.0$ , see Fig. 9) an interesting  
421 change has occurred. While there are two vortices present when only sensible heat is included,  
422 there is only one vortex for case 4. The latent heat flux process reduces surface temperature,  
423 creating a smaller buoyancy force. This natural convection becomes smaller than forced  
424 convection and one vortex remains inside the canyon. This creates a well mixed canyon,  
425 without local inversion layers at the top of the canyon.

*f. Mean radiant temperature*

Next to surface temperature and air temperature, the mean radiant temperature is computed. This is shown in Fig. 10 for different H/W ratios at a height of 2 meter, where  $T_{\text{mrt}}$  is shown for case 3 (excluding latent heat, solid lines) and for case 4 (dash-dotted line). There is no scaling used on the x-axis. For the flat plate, this shows a mean radiant temperature of 345K for case 3. Inclusion of obstacles results in a large variation due to shading. The shadow location is shifted to the right when going from H/W=0.5 to H/W=1.0. The mean radiant temperature in the sunlit part exceeds that of the flat terrain due to multiple reflections and peaks at 355K. For H/W=2.0, there is no direct solar radiation, and all short wave radiation is either diffuse or reflected from obstacles, thereby lowering the amount of absorbed short wave radiation dramatically. This has a large impact on  $T_{\text{mrt}}$ , which decreases down to 270K. Mean radiant temperature is higher at the east part of the canyon for this H/W ratio, due to the multiple short wave reflections that reach this part of the canyon.  $T_{\text{mrt}}$  for H/W=4.0 is as low as 210K, and is not shown in this plot.

If the case including latent heat is considered (dash-dotted lines), lower mean radiant temperatures for all H/W ratios is found. Recall that the case including latent heat for H/W=2.0 did not converge, and is therefore not shown here. For H/W=0.0, this shows a decrease in  $T_{\text{mrt}}$  for the case including latent heat of 2.5K, while the surface temperature dropped by 7.0K in comparison to case 3. The mean radiant temperature is not only a function of surface temperature, but also of sky-based radiation (short wave and long wave emitted from the sky) and therefore shows a smaller change. This difference is however reducing with increasing building height, where H/W=1.0 shows a decrease in surface temperature of 4.2K (averaged over the canyon), while  $T_{\text{mrt}}$  is reduced by 3.0K. This shows that there is a clear relation between surface temperature change and change in mean radiant temperature.

## 4. Discussion

This study focussed on the local day time urban heat island energy budget for an idealized 2D geometry. A transient building-resolving simulation model has been used, which combines radiation, conduction and ventilation at a 1 meter spatial resolution. A range of canyon height to width ( $H/W$ ) ratios and physical mechanisms is considered.

Results showed that the daytime energy budget is dominated by radiation, where absorbed radiation from the sky ( $SW_{\text{dir}}$ ,  $SW_{\text{dif}}$  and  $LW_{\text{sky}}$ ) is the main source of energy at the surface, followed by the long wave trapping effect (energy emitted from the surface and absorbed at an other location). The radiative components are however decreasing with increasing building height, and the other fluxes become more important. The conductive and sensible heat flux are almost zero at the shaded parts of the canyon, while there is a significant contribution of both fluxes at the sunlit part. The sensible heat flux showed two distinct patterns, where for  $H/W > 1.0$  there is one vortex spanning the top of the canyon and a very stable flow situation at the lower part of the canyon. This is due to our 2D case set-up, where cold air can only leave the canyon at roof level. The addition of the latent heat flux process reduces surface temperature and can change the vortex dynamics. For  $H/W = 1.0$  there is only one vortex if the latent heat flux is taken into account, and air temperature remains warmer at street level.

Mean radiant temperature increased for  $H/W = 0.5$  and  $H/W = 1.0$  compared to the flat plate. This is due to the increased multiple reflections of short wave radiation. For deeper canyons, there is no direct sunlight reaching the street level, and mean radiant temperature drops quickly.

The link between surface temperature and mean radiant temperature can be made (at least from a quantitative point of view) relatively easy, since both are largely dependent on radiative properties. The link between surface and air temperature is much harder to make. Air temperature in the canyon is not only dependent on surface temperature, but also on free stream air temperature and wind speed. It was found that there are large

spatial air temperature differences inside the canyon. This makes it difficult to find a proper parametrisation that holds for all  $H/W$  ratios and on every individual canyon surface. This is best displayed for  $H/W=1.0$  for the case with and without latent heat, which shows different vortex dynamics and an increase in air temperature at street level while the surface temperature is decreasing when including the latent heat flux process.

There are some aspects that could be improved in this study, where the most obvious is of course the 2D case set-up. However, going to a 3D case, also comes with more complexity and interplay between all processes, and might therefore create less understanding of the basic phenomena. With the insights gained from this study, the additional effects when going to a 3D environment could be better understood.

Next is the simplification of using buildings which are all spaced equally and have uniform height. The same arguments as for the 2D-geometry can be made. Insight is gained for this simple case, which again comes with the cost of reduced realism.

Apart from these improvement on the case set-up, there are also model improvements, where a large improvement can be made in the CFD model that is used. It is known that the  $k-\epsilon$  model has troubles with strong stratifications due to the assumption of a fully turbulent flow. It might be worth while to investigate other turbulence models (full algebraic stress models) or even a LES-framework. Next to this, the Simple Gradient Diffusion Hypothesis (SGDH) model for the closure of the turbulent heat flux can be improved by using a Generalized Gradient Diffusion Hypothesis (GGDH) or algebraic flux model. This requires more extensive validation of the CFD model, which in turn requires more wind tunnel studies including stratification effects.

The computation of the latent heat flux acts as a sink in the surface energy balance, where a direct feedback is lacking. It could be that a canyon becomes very humid by using the fixed Bowen ratio, but this has no impact on the latent heat flux. It is therefore interesting to solve the full moisture balance, which includes transport of moisture in the ground and obstacles and the transport of moisture through convective transport (using the CFD model). This

505 allows for a latent heat flux that is based on physical mechanisms.

506 *Acknowledgments.*

507 This study is funded by the Dutch Climate Proof Cities consortium, which is part of the  
508 Knowledge For Climate program ([knowledgeforclimate.climate-research-netherlands](https://knowledgeforclimate.climate-research.nl/climateproofcities)  
509 [.nl/climateproofcities](https://knowledgeforclimate.climate-research.nl/climateproofcities)).

## REFERENCES

- 512 Albers, R. A. W., B. Blocken, and P. R. Bosch, 2014: Overview of challenges and achieve-  
 513 ments in the Climate Proof Cities program. *Building and Environment*, manuscript sub-  
 514 mitted for publication.
- 515 Barlow, J., 2014: Progress in observing and modelling the urban boundary layer. *Urban*  
 516 *Climate*, in press.
- 517 De Bruin, H. A. R. and A. A. M. Holtslag, 1982: A simple parameterization of the surface  
 518 fluxes of sensible and latent heat during daytime compared with the penman-monteith  
 519 concept. *Journal Of Applied Meteorology*, **21**, 1610–1621.
- 520 Durbin, P. A., 1996: On the k- $\epsilon$  stagnation point anomaly. *International Journal of Heat*  
 521 *and Fluid Flow*, **17**, 89–90.
- 522 Fiala, D., G. Havenith, P. Brde, B. Kampmann, and G. Jendritzky, 2012: UTCI-Fiala multi-  
 523 node model of human heat transfer and temperature regulation. *International Journal of*  
 524 *Biometeorology*, **56 (3)**, 429–441.
- 525 Grimmond, C. S. B., 2007: Urbanization and global environmental change: local effects of  
 526 urban warming. *Geographical Journal*, **173 (1)**, 83–88.
- 527 Höppe, P., 1999: The physiological equivalent temperature a universal index for the biome-  
 528 teorological assessment of the thermal environment. *International Journal of Biometeo-*  
 529 *rology*, **43**, 71–75.
- 530 Iqbal, M., 1983: *An Introduction To Solar Radiation*. Academic Press.
- 531 Kasten, F., 1996: The linke turbidity factor based on improved values of the integral Rayleigh  
 532 optical thickness . *Solar Energy*, **56 (3)**, 239 – 244.



533 Kenjeres, S. and K. Hanjalic, 1999: Transient analysis of Rayleigh-Benard convection with  
534 a RANS model. *International Journal of Heat and Fluid Flow*, **20** (3), 329 – 340.

535 Kenjeres, S. and K. Hanjalic, 2006: LES, T-RANS and hybrid simulations of thermal con-  
536 vection at high Ra numbers. *International Journal of Heat and Fluid Flow*, **27** (5), 800 –  
537 810.

538 Kenjeres, S. and K. Hanjalic, 2009: Tackling complex turbulent flows with transient RANS.  
539 *Fluid Dynamics Research*, **41** (1), 012 201.

540 Kenjeres, S. and B. ter Kuile, 2013: Modelling and simulations of turbulent flows in urban  
541 areas with vegetation. *Journal of Wind Engineering and Industrial Aerodynamics*, **123**,  
542 **Part A** (0), 43 – 55.

543 Kim, Y.-H. and J.-J. Baik, 2004: Daily maximum urban heat island intensity in large cities  
544 of Korea. *Theoretical and Applied Climatology*, **79** (3-4), 151–164.

545 Klok, L., S. Zwart, H. Verhagen, and E. Mauri, 2012: The surface heat island of rotterdam  
546 dam and its relationship with urban surface characteristics. *Resources, Conservation and*  
547 *Recycling*, **64** (0), 23 – 29, climate Proofing Cities.

548 Klysik, K. and K. Fortuniak, 1999: Temporal and spatial characteristics of the urban heat  
549 island of Lodz, Poland. *Atmospheric Environment*, **33** (24), 3885–3895.

550 Lindberg, F., B. Holmer, and S. Thorsson, 2008: SOLWEIG 1.0 Modelling spatial vari-  
551 ations of 3D radiant fluxes and mean radiant temperature in complex urban settings.  
552 *International Journal of Biometeorology*, **52**, 697–713.

553 Madronich, S., 1987: Photodissociation in the atmosphere: 1. actinic flux and the effects of  
554 ground reflections and clouds. *Journal of Geophysical Research: Atmospheres*, **92** (D8),  
555 9740–9752.

556 Oke, T. R., 1981: Canyon geometry and the nocturnal urban heat island: Comparison of  
557 scale model and field observations. *Journal of Climatology*, **1** (3), 237–254.

558 Peng, S., et al., 2012: Surface urban heat island across 419 global big cities. *Environmental*  
559 *Science & Technology*, **46** (2), 696–703.

560 Prata, A. J., 1996: A new long-wave formula for estimating downward clear-sky radiation at  
561 the surface. *Quarterly Journal of the Royal Meteorological Society*, **122** (533), 1127–1151.

562 Ryu, Y.-H. and J.-J. Baik, 2012: Quantitative Analysis of Factors Contributing to Urban  
563 Heat Island Intensity. *Journal of Applied Meteorology and Climatology*, **51**, 842 – 854.

564 Schmid, H., H. Cleugh, C. Grimmond, and T. Oke, 1991: Spatial variability of energy fluxes  
565 in suburban terrain. *Boundary-Layer Meteorology*, **54** (3), 249–276.

566 Schrijvers, P. J. C., H. J. J. Jonker, S. Kenjeres, and S. R. de Roode, 2014: Breakdown of  
567 the night time urban heat island energy budget. *Building and Environment*, manuscript  
568 submitted for publication.

569 Skartveit, A., J. A. Olseth, and M. E. Tuft, 1998: An hourly diffuse fraction model with  
570 correction for variability and surface albedo . *Solar Energy*, **63** (3), 173 – 183.

571 Steeneveld, G. J., S. Koopmans, B. G. Heusinkveld, L. W. A. van Hove, and A. A. M.  
572 Holtslag, 2011: Quantifying urban heat island effects and human comfort for cities of  
573 variable size and urban morphology in the netherlands. *Journal of Geophysical Research:*  
574 *Atmospheres*, **116** (D20).

575 Taha, H., 1997: Urban climates and heat islands: albedo, evapotranspiration, and anthro-  
576 pogenic heat. *Energy and Buildings*, **25** (2), 99 – 103.

## 577 List of Tables

578	1	Model constants for the standard $k - \epsilon$ model.	27
579	2	Input constants for radiation, heat conduction into the urban material and	
580		the CFD model.	28
581	3	Case set-up, where G is the conductive heat flux process, H the sensible heat	
582		flux process and Le the latent heat flux process.	29

$C_\mu$	$\sigma_k$	$\sigma_\epsilon$	$C_{\epsilon 1}$	$C_{\epsilon 2}$	$C_{\epsilon 3}$
0.09	1.0	1.3	1.44	1.92	1.44

TABLE 1. Model constants for the standard  $k - \epsilon$  model.

Radiation	
Emissivity	0.95
Albedo	0.40
Latitude	52° 22' N
Longitude	4° 53' E
Start day	2012-06-10 00:00
End day	2012-06-20 23:59
Heat conduction	
$\lambda$	0.72 Wm <sup>-1</sup> K <sup>-1</sup>
$\rho$	1920 kgm <sup>-3</sup>
$C_v$	835 Jkg <sup>-1</sup> K <sup>-1</sup>
CFD	
$T_a$	293.15 K
$U$	4.0 m/s
cell width	1.0 m
cell expansion	5 %
max cell size	25 m
$\psi$	1.0

TABLE 2. Input constants for radiation, heat conduction into the urban material and the CFD model.

Case	RAD	G	H	Le
1	+			
2	+	+		
3	+	+	+	
4	+	+	+	+

TABLE 3. Case set-up, where G is the conductive heat flux process, H the sensible heat flux process and Le the latent heat flux process.

## List of Figures

- 1 Eastward flux for direct short wave radiation (top left), eastward flux for  
diffuse short wave radiation (top right), direct short wave flux density for all  
directions (bottom left) and diffuse short wave flux density for all direction  
(bottom right). Input for the direct short wave radiation is  $800 \text{ Wm}^{-2}$  and  
 $100 \text{ Wm}^{-2}$  for the diffuse short wave radiation. 32
- 2 Schematic of case set-up with changing H/W ratio. 14 buildings are spaced  
50 meter apart, while building height (H) is varied. Plotting is done according  
to the inset in the top right. 33
- 3 Time series for the radiative equilibrium case (case 1). The left panel shows  
the surface temperature at one point in the centre of the street canyon for  
different H/W ratios. The right panel shows the summation of absorbed  
radiation from  $SW_{\text{dir}}$ ,  $SW_{\text{dif}}$  and  $LW_{\text{sky}}$ . The dotted lines indicate sunrise and  
sunset, the dashed line the time instance where spatial analysis is conducted  
for. 34
- 4 Absorbed long wave radiation emitted by the sky (top left), absorbed radiation  
due to long wave trapping (top right), total absorbed short wave radiation  
(bottom right) and emitted long wave radiation by walls (bottom left) in case  
of radiative equilibrium (case 1) at mid day (indicated by the dashed line in  
Fig. 3). Plotting is done according to the inset at the top right. 35
- 5 Surface temperature for different H/W ratios (sub plots) and different cases  
(coloured lines). Note the different temperature scale for each sub plot. 36
- 6 Surface fluxes for different H/W ratios (sub plots) and physical mechanisms  
(coloured lines) for case 3 (including conductive and sensible heat flux, but  
excluding latent heat flux). The same scale is used for all plots. 37

608	7	Surface fluxes for $H/W=1.0$ and different physical mechanisms (coloured lines)	
609		for case 3 (excluding latent heat, left panel) and case 4 (including latent heat,	
610		right panel).	38
611	8	Air temperature (K) and velocity vectors for case 3 (excluding latent heat)	
612		for different $H/W$ ratios. Note the different temperature scales.	39
613	9	Air temperature (K) and velocity vectors for $H/W=1.0$ for case 4 (including	
614		latent heat). The colour scale used is the same as for case 3.	40
615	10	Profiles of mean radiant temperature at $z=2\text{m}$ height between canyon 12 and	
616		13 for case 3 (excluding latent heat, solid lines) and case 4 (including latent	
617		heat, dash-dotted line). Note that $H/W=4.0$ is not shown here.	41



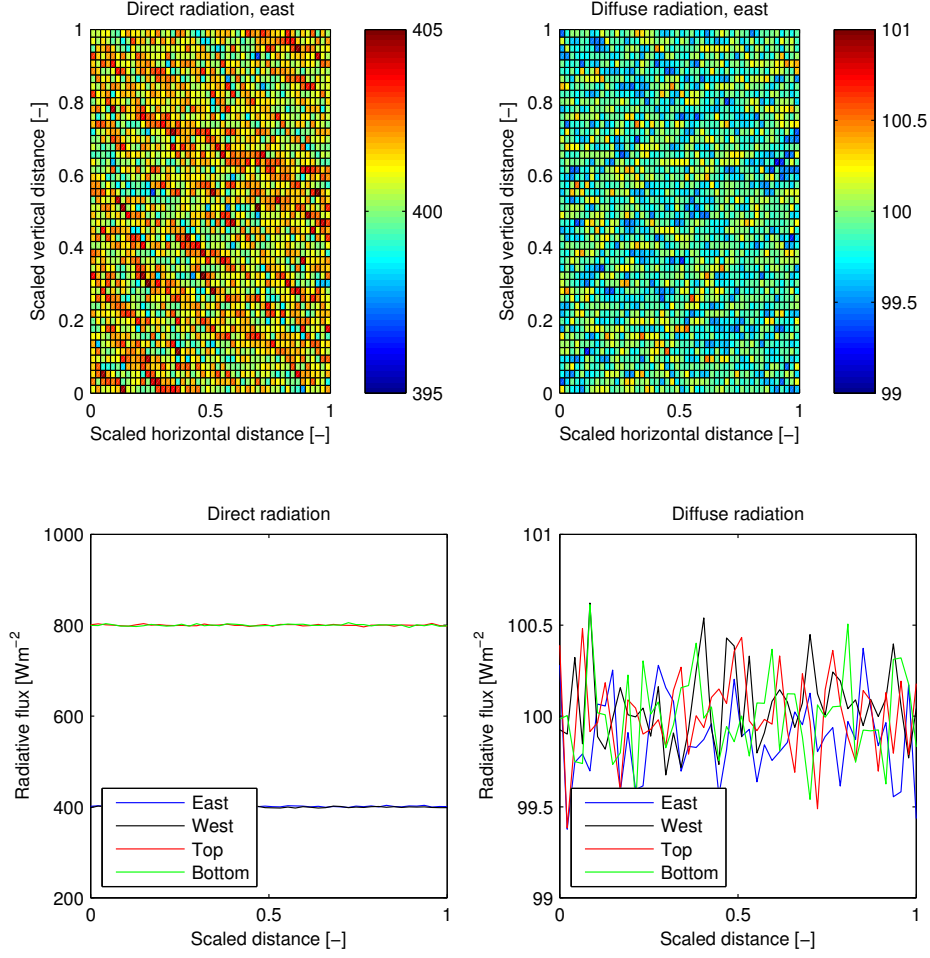


FIG. 1. Eastward flux for direct short wave radiation (top left), eastward flux for diffuse short wave radiation (top right), direct short wave flux density for all directions (bottom left) and diffuse short wave flux density for all direction (bottom right). Input for the direct short wave radiation is  $800 \text{ Wm}^{-2}$  and  $100 \text{ Wm}^{-2}$  for the diffuse short wave radiation.

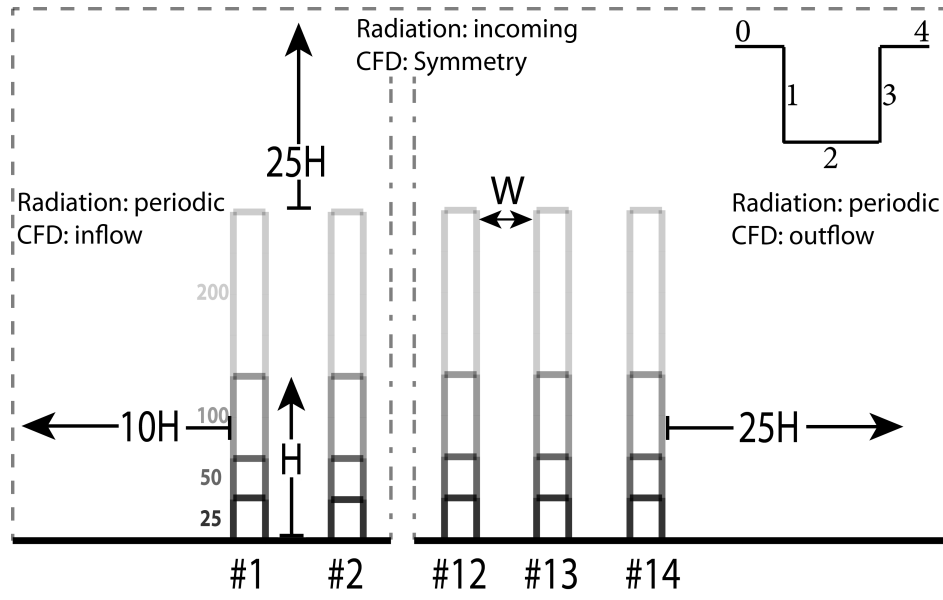


FIG. 2. Schematic of case set-up with changing  $H/W$  ratio. 14 buildings are spaced 50 meter apart, while building height ( $H$ ) is varied. Plotting is done according to the inset in the top right.

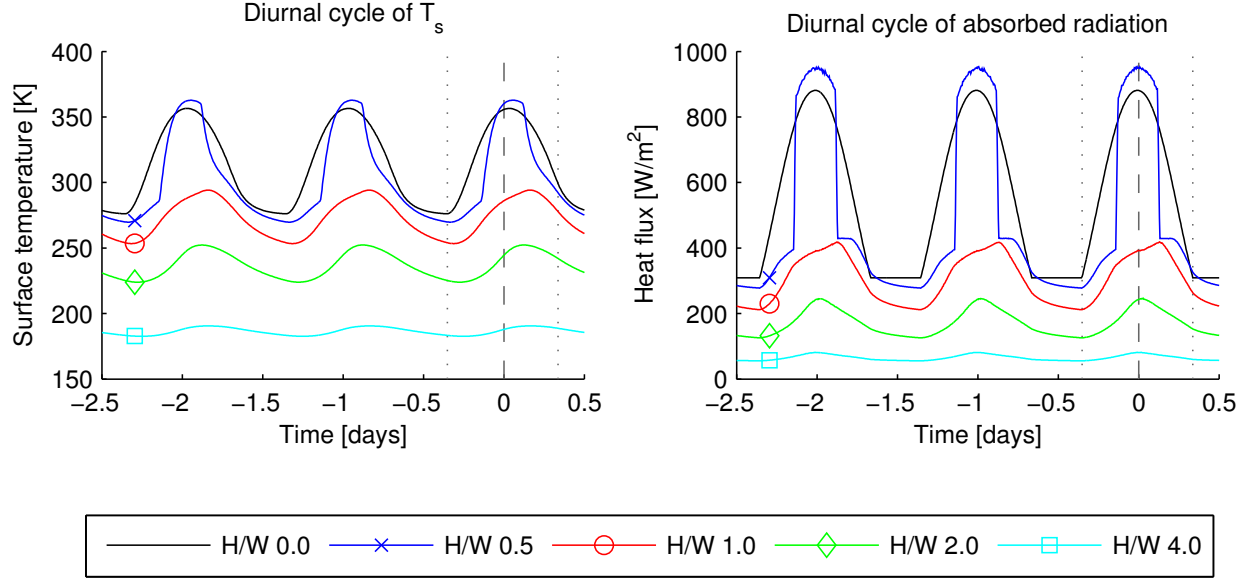


FIG. 3. Time series for the radiative equilibrium case (case 1). The left panel shows the surface temperature at one point in the centre of the street canyon for different H/W ratios. The right panel shows the summation of absorbed radiation from  $SW_{\text{dir}}$ ,  $SW_{\text{dif}}$  and  $LW_{\text{sky}}$ . The dotted lines indicate sunrise and sunset, the dashed line the time instance where spatial analysis is conducted for.

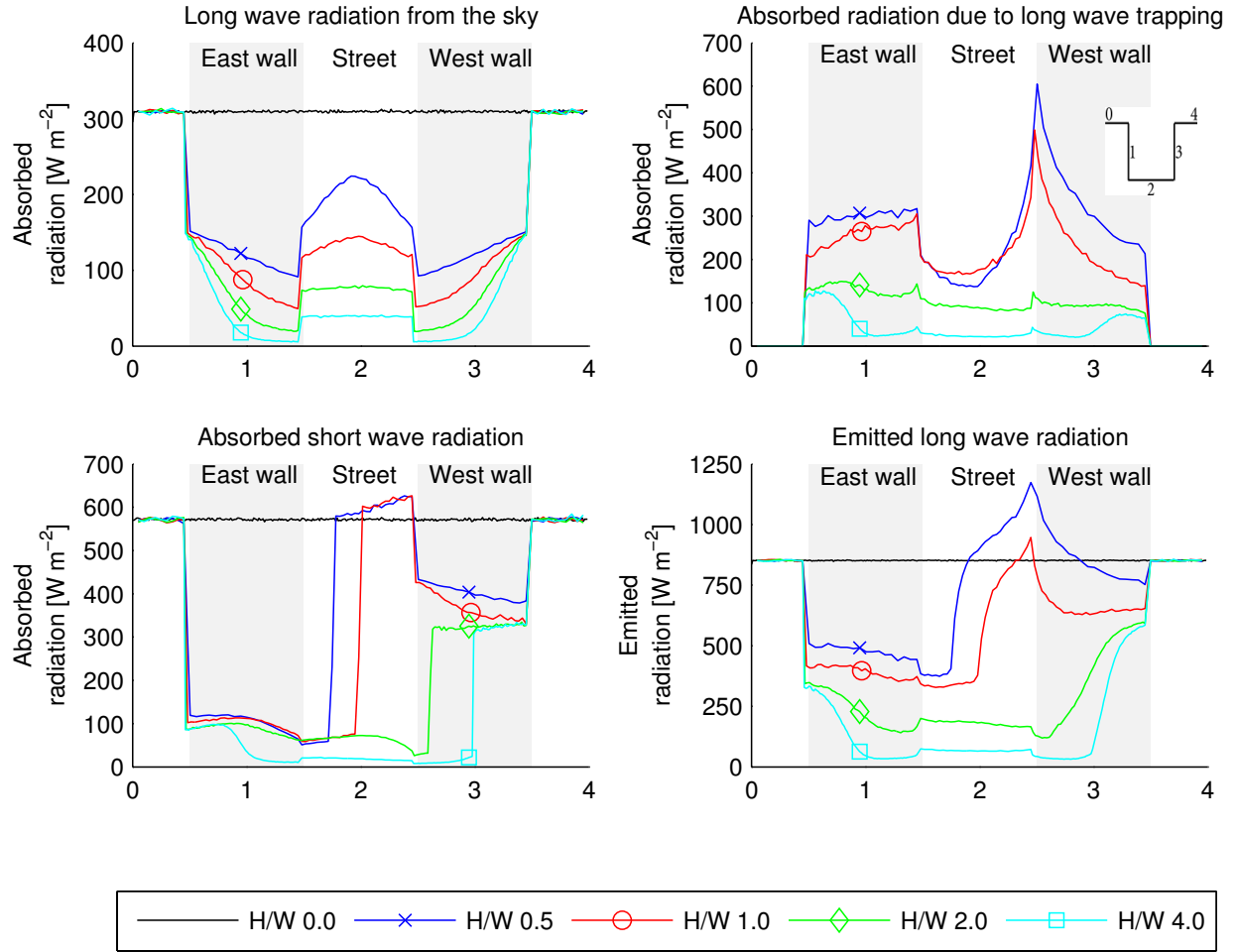


FIG. 4. Absorbed long wave radiation emitted by the sky (top left), absorbed radiation due to long wave trapping (top right), total absorbed short wave radiation (bottom right) and emitted long wave radiation by walls (bottom left) in case of radiative equilibrium (case 1) at mid day (indicated by the dashed line in Fig. 3). Plotting is done according to the inset at the top right.

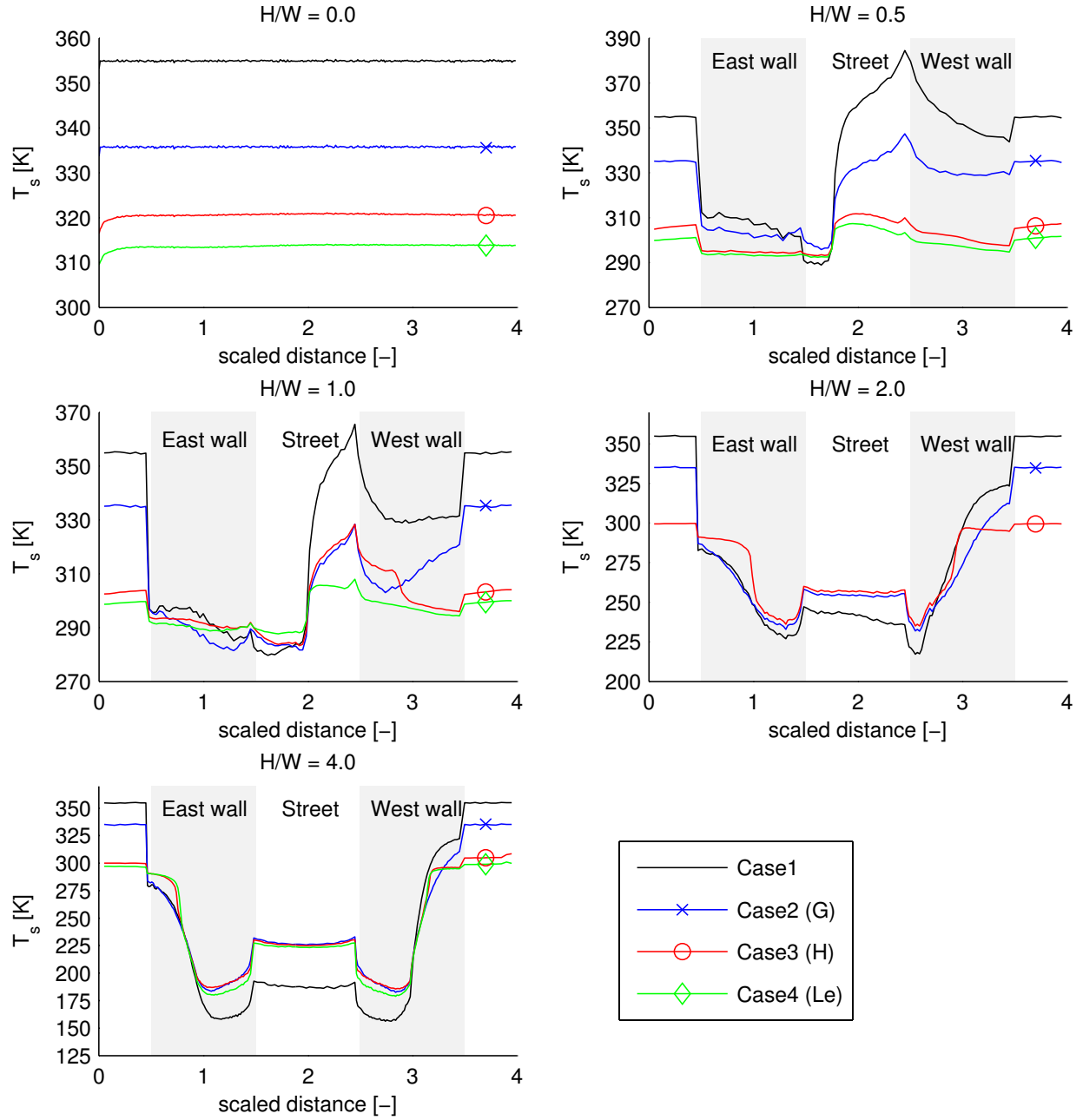


FIG. 5. Surface temperature for different  $H/W$  ratios (sub plots) and different cases (coloured lines). Note the different temperature scale for each sub plot.

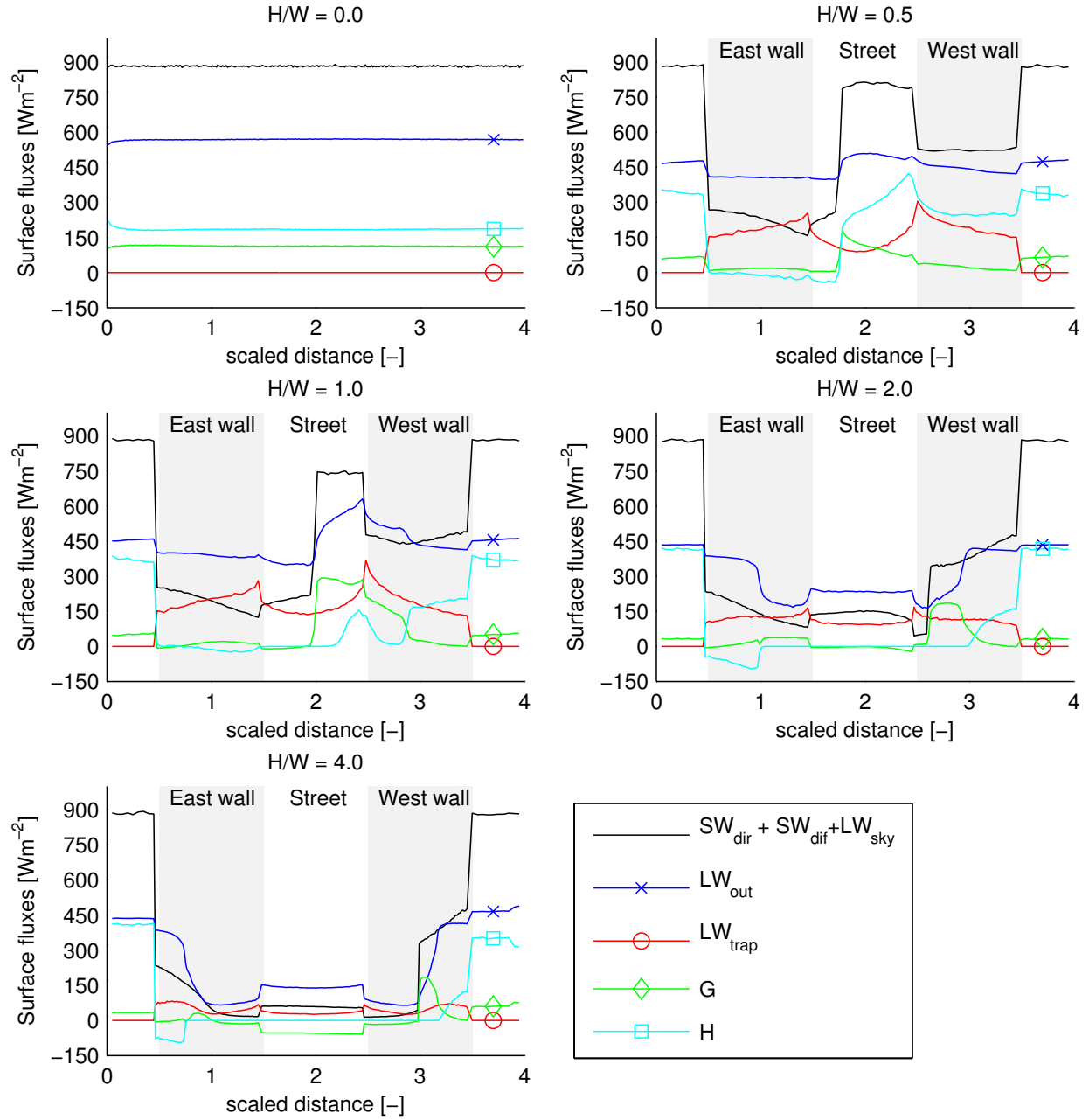


FIG. 6. Surface fluxes for different  $H/W$  ratios (sub plots) and physical mechanisms (coloured lines) for case 3 (including conductive and sensible heat flux, but excluding latent heat flux). The same scale is used for all plots.

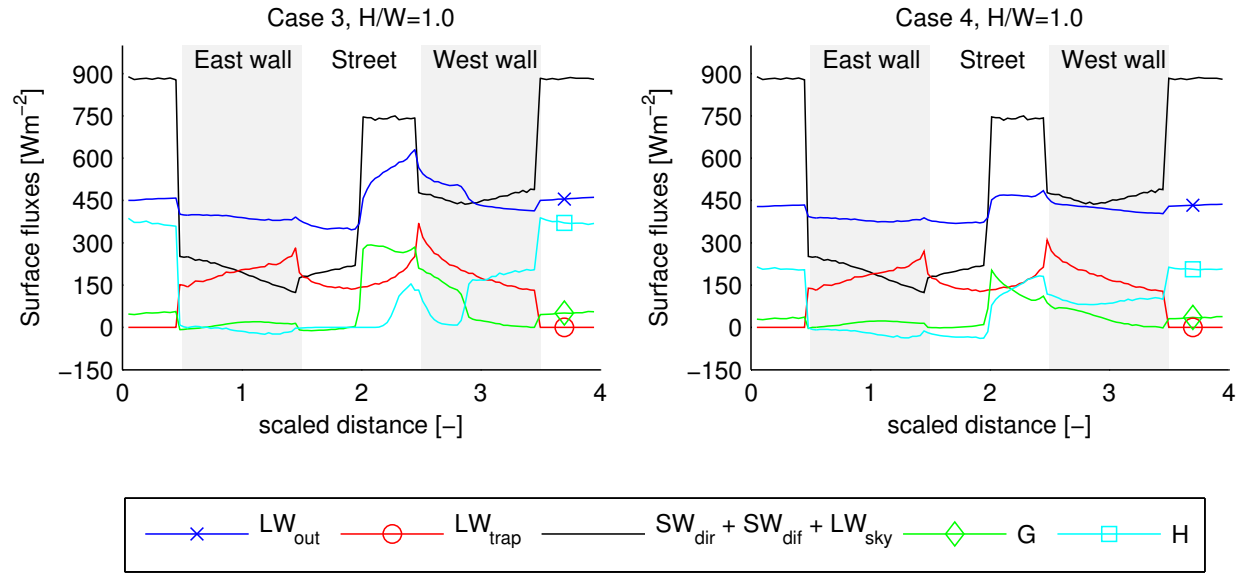


FIG. 7. Surface fluxes for  $H/W=1.0$  and different physical mechanisms (coloured lines) for case 3 (excluding latent heat, left panel) and case 4 (including latent heat, right panel).

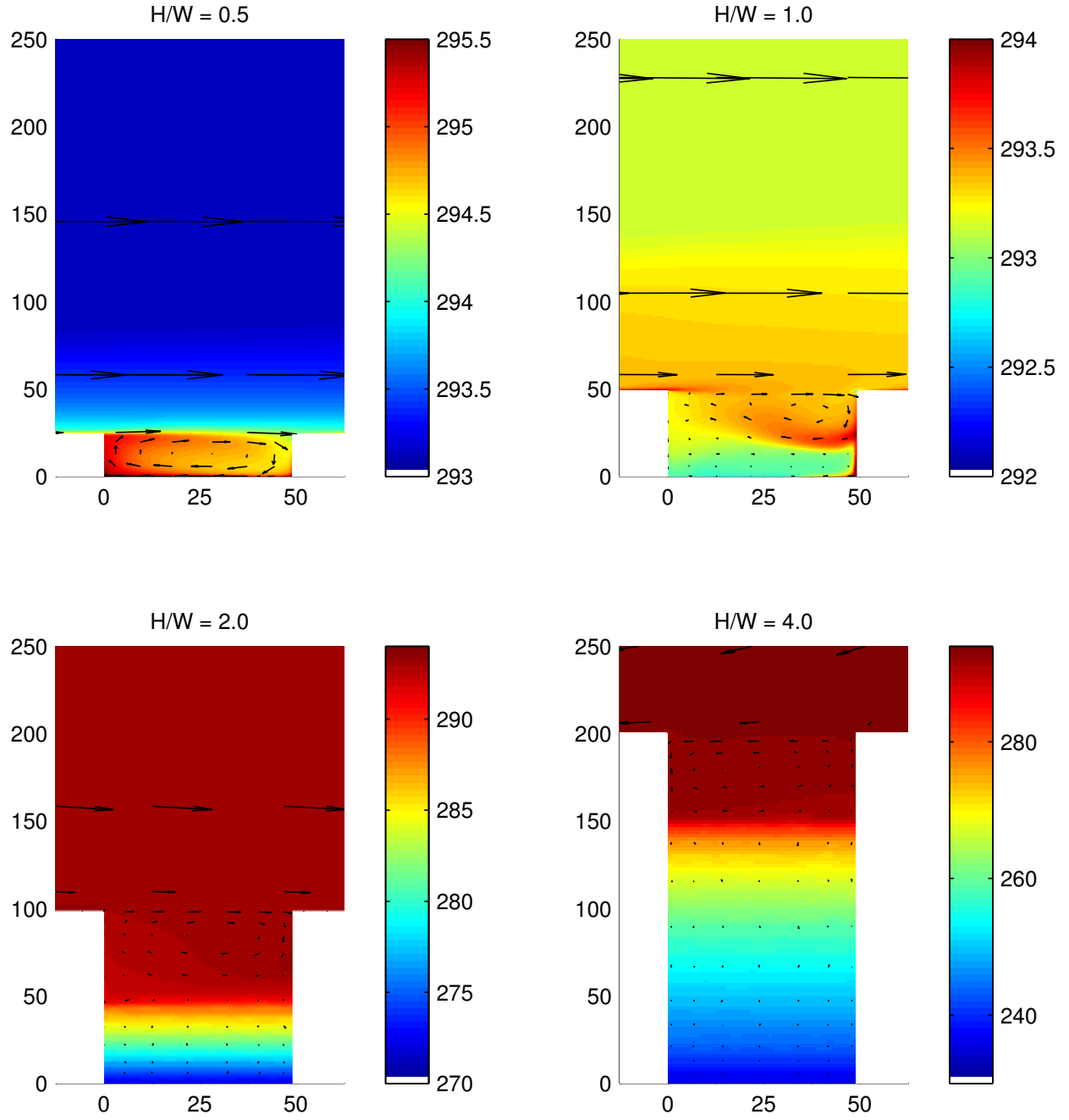


FIG. 8. Air temperature (K) and velocity vectors for case 3 (excluding latent heat) for different H/W ratios. Note the different temperature scales.



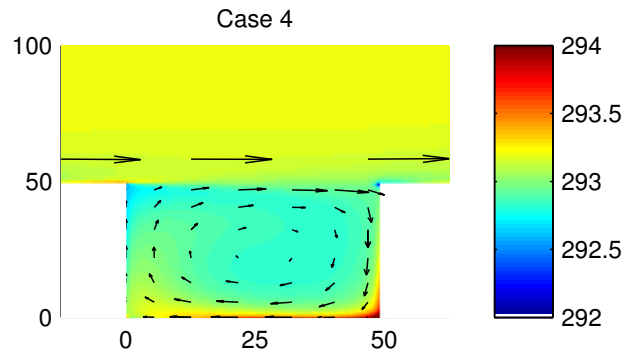


FIG. 9. Air temperature (K) and velocity vectors for  $H/W=1.0$  for case 4 (including latent heat). The colour scale used is the same as for case 3.

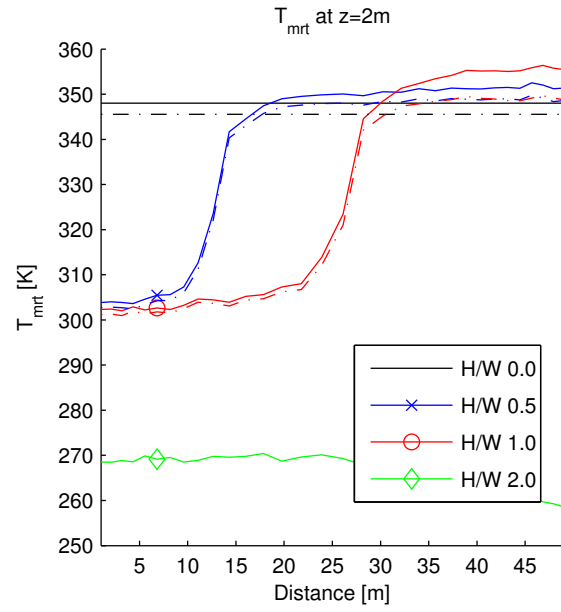


FIG. 10. Profiles of mean radiant temperature at  $z=2\text{m}$  height between canyon 12 and 13 for case 3 (excluding latent heat, solid lines) and case 4 (including latent heat, dash-dotted line). Note that  $H/W=4.0$  is not shown here.